ACSNANO

www.acsnano.org

ARTICLE

Growth Twinning and Generation of High-Frequency Surface Nanostructures in Ultrafast Laser-Induced Transient Melting and Resolidification

Xxx Sedao,[†,⊥] Maxim V. Shugaev,[‡,⊥] Chengping Wu,[‡] Thierry Douillard,[§] Claude Esnouf,[§] Claire Maurice,[∥] Stéphanie Reynaud,[†] Florent Pigeon,[†] Florence Garrelie,[†] Leonid V. Zhigilei,[‡] and Jean-Philippe Colombier*[,†]

[†]Univ Lyon, UJM-Saint-Etienne, CNRS, IOGS, Laboratoire Hubert Curien UMR5516, F-42023 St-Etienne, France

[‡]Department of Materials Science and Engineering, University of Virginia, 395 McCormik Road, Charlottesville, Virginia 22904-4745, United States

[§]Univ Lyon, INSA Lyon, CNRS, MATEIS, UMR 5510, F-69621 Villeurbanne, France

[∥]Ecole Nationale Supérieure des Mines de Saint-Etienne, Laboratoire Georges Friedel, CNRS, UMR5307, 42023 St-Etienne, France

ABSTRACT: **The structural changes generated in surface regions of single crystal Ni targets by femtosecond laser irradiation are investigated experimentally and computationally for laser fluences that, in the multipulse irradiation regime, produce sub-100 nm high spatial frequency surface structures. Detailed experimental characterization of the irradiated targets combining electron back scattered diffraction analysis with high-resolution transmission electron microscopy reveals the presence of multiple nanoscale twinned domains in the irradiated surface regions of single crystal targets with (111) surface orientation. Atomistic- and continuum-level simulations performed for experimental irradiation conditions reproduce the generation of twinned domains and establish the conditions leading to the formation of growth twin boundaries in the course of the fast transient melting and epitaxial regrowth of the surface regions of the irradiated targets. The observation of growth twins in the irradiated Ni(111) targets provides strong evidence of the role of surface melting and resolidification in the formation of high spatial frequency surface structures. This also suggests that the formation of twinned domains can be used as a sensitive measure of the levels of liquid undercooling achieved in short pulse laser processing of metals.**

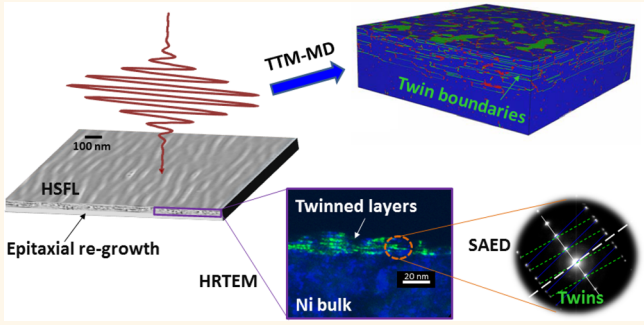

KEYWORDS: *ultrafast laser, transient melting and resolidification, laser-induced lattice defects, growth twin, laser-induced periodic surface structures, high-frequency surface nanostructures*

High-precision machining of materials with ultrashort laser pulses[1−3] is a powerful enabling technology actively used in a broad range of applications in the fields of photonics, biomedical and life sciences.[4−6] The preparation and functionalization of material surfaces on the nanometer scale are of prime importance for the advancement of these applications. Micro and nanostructural changes strongly impact surface properties such as optical reflectivity, hydrophobicity, hardness, wear and corrosion resistance, potentially impacting the use of the treated materials.[7−9] Laser-induced surface modification is the result of material response to the extreme conditions of rapid highly localized heating and cooling created in the surface region of irradiated targets by ultrafast laser irradiation. Under multipulse exposition, high densities of crystal defects and subsurface voids can be accumulated during successive thermomechanical loading of the material leading to irreversible surface damage and ablation.[10−17]

Interaction of an ultrashort laser pulse with a metal surface starts from the transient absorption of incident photons by the conduction band electrons, which leads to a sharp rise of the electron temperature. The hot electrons then conduct energy

Received: May 4, 2016
Accepted: July 7, 2016
Published: July 7, 2016

DOI: 10.1021/acsnano.6b02970
ACS Nano 2016, 10, 6995−7007

deeper into the irradiated target and, on the picosecond time scale, thermalize with the lattice through electron−phonon coupling.[18] The lattice heating leads to the rapid melting and resolidification, spallation, ablation, and generation of crystal defects occurring on the time scale of hundreds of picoseconds to nanoseconds. Depending on the laser fluence and material properties, the laser-induced processes may include complex hydrodynamic motion and material redistribution in the surface region of the irradiated target[19−22] as well as generation of unusual microstructure in the subsurface region.[17]

At low fluences, in the "submelting" regime, laser irradiation could cause material damage through thermal stresses.[13] After repetitive irradiation, the accumulated damage manifests itself through the formation of slip bands, increase in the surface roughening, and corresponding reflectivity changes.[14,15] At higher fluences, a thin surface layer may undergo rapid melting followed by epitaxial resolidification,[23] leading to the generation of a high density of crystal defects, such as vacancies, dislocations, stacking faults and twin boundaries.[16,24,25] Further increase in laser fluence can lead to more extensive microstructural changes and modifications of surface morphology, including the generation of subsurface voids trapped by rapidly advancing solidification front,[17] formation of a nanocrystalline surface layer, or surface nanospikes featuring pentagonal twinned structural elements.[17,26] The microstructural changes in this regime can extend down to a substantial depth under the irradiated surface, with laser-induced shear stresses producing deformation twins and dislocations far below the region experiencing laser melting and ablation.

While single pulse irradiation can readily alter the surface topography, multiple-pulse irradiation can cause interference between the incident laser light and surface scattered electromagnetic waves, potentially involving surface plasmon excitation,[27−30] thus giving rise to periodic modulation of surface morphology with periods close to the laser wavelength, known as Laser-Induced Periodic Surface Structures (LIPSS), or more accurately, Low Spatial Frequency LIPSS (LSFL).[28] Unlike the defects generated under a flat surface, the defects distribution in LSFL appears to be anisotropic.[31] In fact, the defect generation seems to compete with LSFL formation, with both processes exhibiting sensitivity to the crystallographic orientation of the irradiated surface.[32] At somewhat lower laser fluences, another kind of LIPSS with a periodicity significantly smaller than the laser wavelength, down to $\Lambda \approx \lambda/10$, can be produced. These surface structures are often referred to as High Spatial Frequency LIPSS (HSFL) and can be oriented parallel or perpendicular to the laser polarization.[33,34] The origin of such structures is much less understood and a number of alternative mechanisms have been proposed, including the coherent superposition of scattered and refracted waves,[29] laser-induced surface plasma waves,[35,36] surface oxidation and higher harmonic generation,[37] surface self-organization,[38] and coherent nanobubble formation in the subsurface region.[39,40] One general question of fundamental importance is whether the HSFL formation is essentially associated with phase transformations triggered by ultrafast laser irradiation. Since the contrast of HSFL is relatively weak, and the time of the laser melting and resolidification can be very short,[23,41,42] the direct time-resolved probing of the laser-induced processes is difficult.[41−44] Nevertheless, a reliable interpretation to the results from *ex situ* analysis of laser-processed samples requires an improved understanding of the connections between the rapid highly nonequilibrium phase transformations and the ensuing surface modifications produced by the laser irradiation.

In this paper, we combine a detailed experimental characterization of single crystal Ni targets irradiated in the regime where HSFL are produced with a thorough computational and theoretical analysis of laser-induced melting and resolidification processes. The generation of growth twin boundaries is found to be a clear indicator of the role of melting and a sensitive measure of the degree of undercooling reached at the solidification front in laser interactions with Ni(111) targets.

RESULTS AND DISCUSSION

Experiment Results. Figure 1 presents the surface morphology of a Ni(111) crystal after irradiation by 46 laser pulses at 0.19 J/cm^2, a level of incident fluence that, when converted to the absorbed fluence using reflectivity of 0.7,[45] exceeds the melting threshold predicted in atomistic simulations. The scanning electron microscopy (SEM) image shows the formation of HSFL in the 5 μm wide central part of the laser spot. An enlarged view of the area outlined by the dashed box is shown as an inset to highlight the morphology of the HSFL. The periodicity of the HSFL was measured on SEM micrographs and further confirmed by Fourier transform (FT) of the images. A two-dimensional FT spectrum analysis of the SEM images asserts the periodicity of the HSFL is Λ = 70−90 nm. Although HSFL are mainly observed in the direction parallel to the laser polarization, the individual ridges are not continuous but terminate quasi-randomly within the HSFL. A few nanocavities, which might have been formed due to subsurface cavitation,[17] are visible on the HSFL ridges. The peak-to-valley amplitude of the HSFL was assessed by atomic force microscopy (AFM) to be about 20 nm. The surface roughness outside the central HSFL area remains as flat as the one of the polished sample.

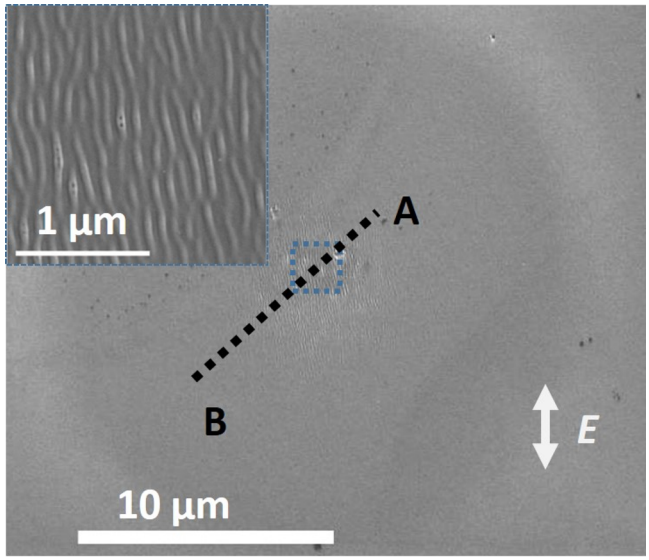

Figure 1. SEM image of a Ni(111) crystal irradiated by 46 laser pulses at an incident laser fluence of 0.19 J/cm^2. An enlarged view of the area outlined by the dashed line is shown as an inset in the upper-left corner. The black dotted line A−B shows the location of the lamella extraction for the cross-sectional analysis illustrated in Figures 3, 4, 5a. The laser polarization *E* is indicated by the white arrow.

DOI: 10.1021/acsnano.6b02970
ACS Nano 2016, 10, 6995−7007

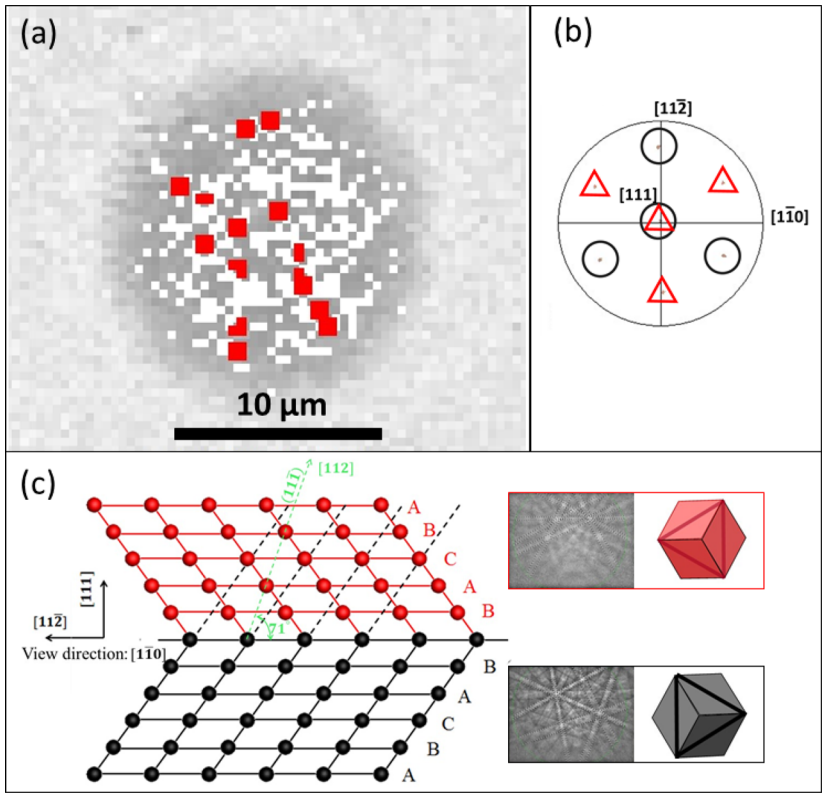

Figure 2. Crystal structure modification in the central area of the laser spot on a Ni(111) crystal irradiated by 46 laser pulses at an incident laser fluence of 0.19 J/cm^2. (a) EBSD map reflects the lattice distortions due to the presence of crystal defects (the greyer the larger are the distortions) and twins (red-colored spots) in the central area of the laser impact. The white-colored zones in the center of the map are the areas where EBSD indexing was not possible. (b) ⟨111⟩ pole figure from EBSD indexed crystal orientations showing the projection of the original ⟨111⟩ axes (indicated by black circles) along with the new ⟨111⟩ axes appearing due to laser-induced growth twinning (indicated by red triangles). (c) Schematic representation of atomic structure in the vicinity of a twin boundary (left panel) and Kikuchi patterns obtained from nonirradiated surface (lower right panel) and a twinned region generated by laser irradiation (upper right red panel). The corresponding cube presentations of a fcc unit cell, with (111) planes highlighted and common [111] axis pointing out from the paper plane, are also shown next to the Kikuchi patterns for the original and twined crystals.

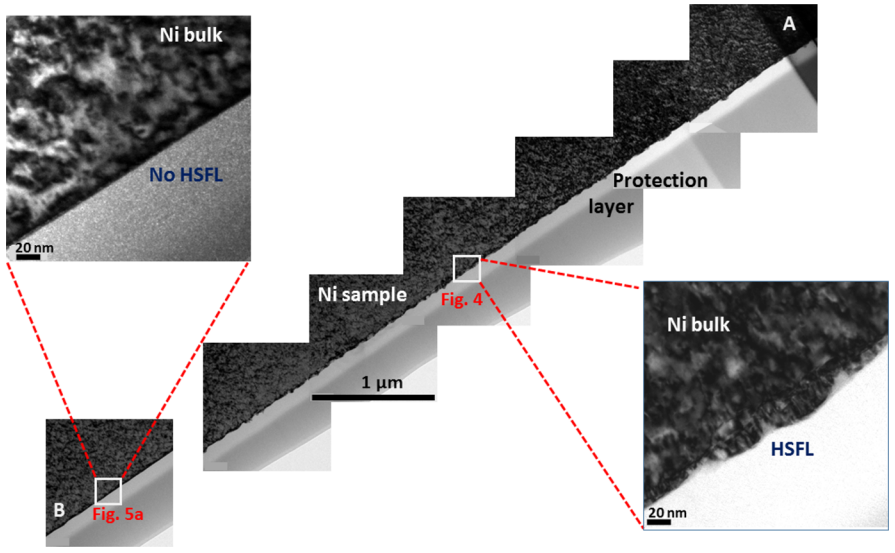

Figure 3. Results of cross-sectional study of a Ni(111) crystal irradiated by 46 laser pulses at an incident laser fluence of 0.19 J/cm^2. A series of TEM images from the lamellae extracted by a site specific method using FIB are composed together to make a montage that corresponds to zone A−B in Figure 1. The two areas outlined by white rectangles are enlarged and further analyzed in Figures 4 and 5a.

The laser-induced generation of crystal defects is characterized with electron backscatter diffraction (EBSD) and illustrated in Figure 2a. At the center of the laser spot, an area with a diameter of 15 μm rendered with dark-gray color has a higher degree of lattice distortion. The localized white-color coded areas in the central part of the laser spot are places

DOI: 10.1021/acsnano.6b02970
ACS Nano 2016, 10, 6995−7007

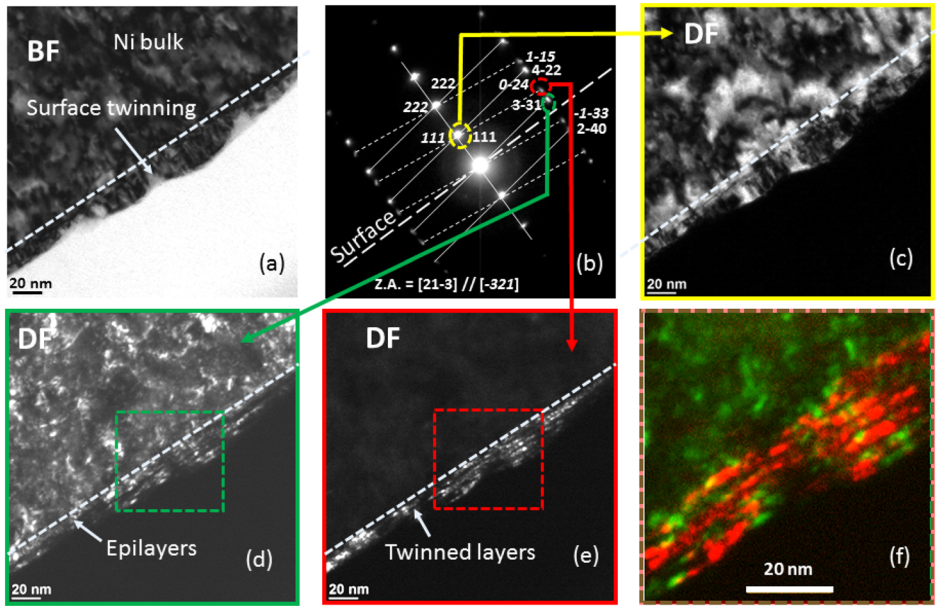

Figure 4. Results of detailed microscopy examination of the central area marked in Figure 3. (a) BF image. (b) Selected area electron diffraction (SAED) showing two superimposed diffraction patterns: one highlighted by solid white lines with zone axis $[21\bar{3}]$ and diffraction spots indexed in nonitalic characters and another highlighted by thin dashed white lines with zone axis $[\bar{3}21]$ and diffraction spots indexed in italic. Note the mirror symmetry with respect to the common (111) plane, *i.e.*, the initial surface of Ni substrate. Selected diffraction spots (111), $(3\bar{3}1)$, and $(0\bar{2}4)$ were used to obtain DF images shown in (c), (d), and (e), respectively. In (c), the bulk of the crystal, epilayers, and twinned domains can be identified. In (d), the bulk of the crystal and the epitaxial layers are revealed. In (e), the complementary details attributed to twinned domains can be seen. The thick dashed white lines in BF and DF images are visual guides outlining the surface region where the laser-induced twinning occurred. The areas marked by the green and red boxes in (d) and (e) are enlarged, superimposed and illustrated in (f). (f) False color image highlighting the spatial distribution of the epilayers (green) and twinned domains (red).

without successful EBSD indexing, which is also related to the generation of crystal defects.[32] One type of crystal defects that is prominently present within the irradiated area is the twin boundary. The twins are identified through EBSD indexing in the regions highlighted by the red color in Figure 2a. The EBSD ⟨111⟩ pole figure generated from the same surface region is displayed in Figure 2b, which sums up the orientation relationship between the lattice of original orientation and twinned lattice. The pole figure manifests clearly the projection of the twinned ⟨111⟩ axes in addition to the ⟨111⟩ axes of the original crystal. A schematic representation of the atomic arrangement in the vicinity of a twin boundary is provided in Figure 2c. The areas where the twinning is recorded with a sufficient intensity are highlighted by red color in Figure 2a. For EBSD indexation of twins, a substantial twinned volume is required to generate Kikuchi patterns typical of twinned domains, as shown in Figure 2c. The EBSD Kikuchi patterns and corresponding cube representations of the atomic arrangements (for the sake of conciseness the atoms in the face-centered cubic (fcc) unit cells are not drawn) are shown for the pristine and twinned lattices in the bottom-right and top-right corners of Figure 2c, respectively. These insets illustrate that the lattice misorientation across a coherent Σ3 {111} twin boundary can be described as 60° rotation around the [111] axis. Some of the Kikuchi bands of the original lattice also appear in the EBSD pattern for twinned domain, but they are faint compared to the twinned ones, indicating some degree of overlap or interlay between the lattice of original orientation and twinned domains. The laser-induced generation of twins, inferred from the EBSD analysis, is further confirmed and visualized in the cross-sectional study of laser-modified surface layers described below.

In order to investigate the microstructure generated beneath the HSFL and the neighboring flat region, a 10 μm long lamella is extracted from the central area of the laser spot marked by the dotted-line A–B in Figure 1 by the standard focused ion beam (FIB) lift-out process. An assembly of the TEM images along the lamella is provided in Figure 3. The HSFL look elongated due to the 45° cut with respect to the HSFL alignment. For the sake of being concise and representative, only images illustrating typical morphologies are given in Figure 3. The flat portion of the surface between the central region and B-end of the lamella is left out in Figure 3. Two representative local sites in the central HSFL region and in the off-center flat surface region near the B-end are marked by white boxes in Figure 3 and imaged via high-resolution transmission electron microscopy (TEM) bright field (BF) mode, as shown in the insets in Figure 3. These locations are chosen for high-resolution examination reported in the following paragraphs.

Figure 4 shows high resolution TEM images on the central part of the laser spot. The BF image (Figure 4a) gives an overview of the zone of interest. Figure 4b is the electron diffraction pattern generated from the HSFL and its subsurface region. It reveals the characteristic signature of twinning, with two sets of diffraction patterns emanating from the original lattice and twinned lattice. The yellow dashed-line oval highlights the common (111) diffraction spot shared between the two lattices, as illustrated in Figure 2. The diffraction spot $(3\bar{3}1)$ is attributed to the original lattice and is enclosed by the green dashed-line oval. The new (twinning) diffraction spot $(0\bar{2}4)$ is outlined by the red dashed-line oval. The diffraction spots in Figure 4b are attributed exclusively to the Ni crystal, *i.e.*, no signs of oxidation and formation of NiO_x or Ni-related

DOI: 10.1021/acsnano.6b02970
ACS Nano 2016, 10, 6995–7007

amorphous material are observed in this region. The three diffraction spots marked in Figure 4b are chosen to generate dark field (DF) images that are color-boxed (in yellow, green and red) and presented in Figure 4c–e, respectively. The DF image taken based on the common (111) diffraction spot (Figure 4c) appears as a matching pair to the BF image (Figure 4a). The $(3\bar{3}1)$ DF image yields a full view of the bulk and six to eight rows of laminated epilayers of lattice with original crystal orientation grown parallel to the surface. In the $(0\bar{2}4)$ DF image, another six to eight complementary rows of laminated twin layers are revealed. These roughly equally spaced layers are 4–5 nm thick and add up to a total of about 30 nm thick surface region. In order to depict the spatial distribution of the epilayers and twins, a small central region is selected from Figure 4d and e (indicated by the dashed-line boxes), the two images of this region are superimposed and represented using false colors in Figure 4f. The mechanisms responsible for the generation of the twinned structure will be elucidated below, with the aid of computational modeling.

We notice that the formation of a 30 nm thick region featuring multiple twinned domains is observed in the central part of the laser spot, where HSFL are formed. In contrast, the $(0\bar{2}4)$ DF image taken from the off-center region (see Figure 3) and shown in Figure 5a reveals the presence of a single sheet of

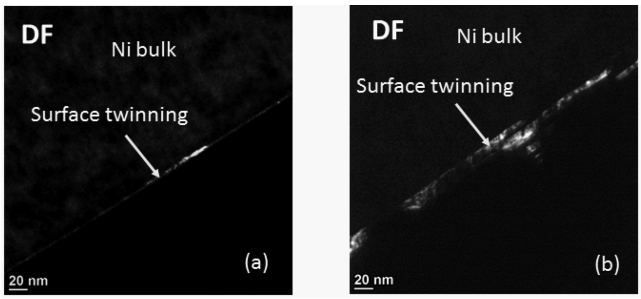

Figure 5. Results of detailed microscopy inspection of cross-section samples: (a) $(0\bar{2}4)$ DF image of the peripheral area marked B in Figure 3 (same operating conditions as in Figure 4e). (b) $(0\bar{2}4)$ DF image evidencing twin formation in the central part of a spot irradiated by two laser pulses at a higher incident fluence of 0.38 J/cm^2. Compared to irradiation at a lower fluence of 0.19 J/cm^2 (Figure 4e), the thickness of the twinned layers is greater here.

5 nm-thick twinned domain. The difference in the number of twinned domains between the center and off-center regions appears to be related to the difference in the local laser fluence, but not to the number of laser pulses. It is also evident that the surface is smooth and flat, and HSFL are not present in this peripheral area.

In order to further illustrate the role the laser fluence plays in the formation of twins, control experiments were carried out for a Ni(111) target irradiated by two laser pulses at 0.38 J/cm^2, an incident fluence level just below the single-shot ablation threshold. At this fluence, HSFL were generated by the 2-pulse irradiation, and material removal in the center of the laser spot was measured to be less than a few nanometers. The EBSD surface analysis reveals the presence of twinned domains in the part of the laser spot where the local fluence produced by the Gaussian laser beam exceeds the melting threshold. The cross-sectional DF image from the center of the laser spot, shown in Figure 5b, confirms the presence of twinned layers: two to four layers can be identified with the thickness of each twinned domain exceeding 10 nm. As compared to the lower fluence case (Figure 4e), the total numbers of twinned layers and the epilayers are smaller, while the thickness of each layer is greater. The total thickness of the surface region exhibiting layered twinned structure, measured at a slightly off center site without the HSFL presence, was found to be larger than 40 nm. It appears, therefore, that a relationship exists between the local laser fluence and the thickness of the twinned domains and epilayers. The physical origin of this relationship is related to the laser fluence dependence of the undercooling conditions achieved during the resolidification process, as discussed in detail later on the basis of TTM calculations.

With the same experimental conditions used for (111) surfaces, a second control experiment was carried out on a single crystal Ni target with (100) surface orientation. No twins were observed, either by the EBSD surface analysis or cross-section TEM examination. This null result confirms that the ultrafast laser-induced lattice defect formation is crystal orientation dependent[32] and agrees with predictions of large scale TTM-MD simulations performed for Ni targets with (100), (011), and (111) surface orientations and presented in the next section.

The laser-induced lattice twinning has also been observed for a Cu target irradiated by a single 6.7 ps laser pulse at a fluence close to the threshold for surface modification.[46] While the formation of twins was attributed in ref 46 to thermal stresses and plastic deformation, the localization of the twinned domains within the top 50–60 nm layer under the irradiated surface, *i.e.*, within the region that likely experienced melting and resolidification, as well as the close-to-parallel orientation of twins with respect to the irradiated surface, which implies low shear stresses resolved on the twinning planes, suggest that an alternative mechanism may be responsible for twinning. The results of a thorough computational and theoretical analysis presented in the next section provide strong evidence that the twinned domains observed in the experimental studies are generated through the growth twinning occurring in the course of transient melting and epitaxial regrowth of the surface regions of the irradiated targets.

Computational and Theoretical Analysis. The mechanisms and kinetics of laser-induced melting and resolidification of Ni targets are investigated in atomistic and continuum-level simulations performed for irradiation conditions used in the experiments. A single-pulse irradiation is considered in the simulations to evaluate the nature of material modification in one excitation–relaxation cycle. The atomic-level mechanisms responsible for the generation of surface microstructure in the course of rapid solidification of transiently melted surface regions are studied in a series of large-scale atomistic simulations, whereas a quick scan of the undercooling conditions created by the laser irradiation at different laser fluences is performed with a continuum model. The mechanisms of the experimentally observed generation of a high density of twin boundaries in the surface regions of single crystal Ni targets irradiated by femtosecond (fs) laser pulses are discussed in this section based on the results of large-scale atomistic simulations of laser interactions with Ni targets, theoretical analysis of the generation of growth twins in the course of rapid solidification under conditions of strong undercooling, and continuum-level modeling of laser-induced melting and resolidification of Ni targets at different laser fluences.

Observation of Laser-Induced Twinning in Large-Scale Atomistic Simulations. The general picture of the laser-

DOI: 10.1021/acsnano.6b02970
ACS Nano 2016, 10, 6995–7007

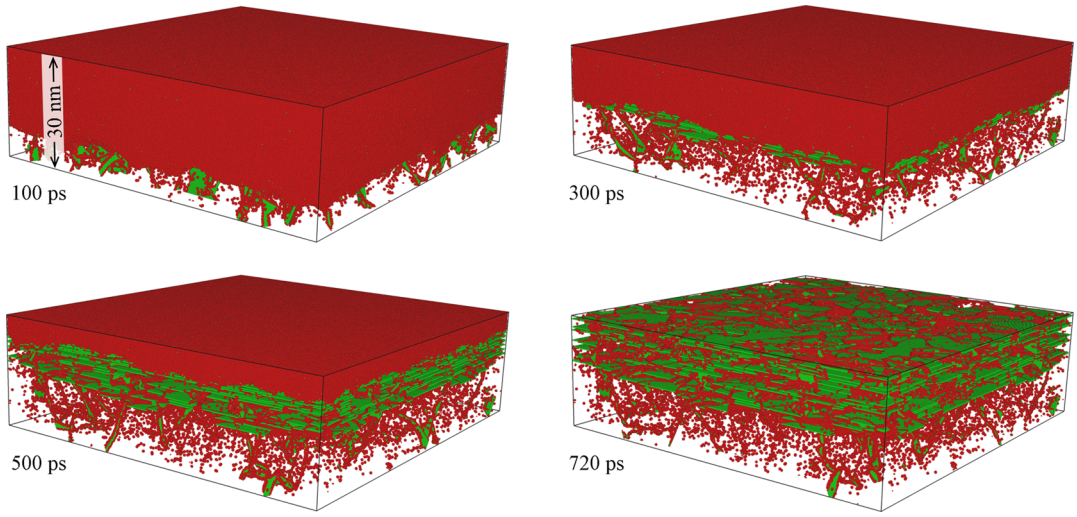

Figure 6. Snapshots of atomic configurations generated in a TTM-MD simulation of a Ni(111) target irradiated by a 50 fs laser pulse at an absorbed fluence of 0.06 J/cm^2. Only the top 30 nm surface region of the irradiated target is shown in the snapshots. The atoms with local structural environment characteristic of fcc crystal structure are blanked to expose the defect structures. The remaining atoms are colored by their local structural environment, so that the green atoms have local structure characteristic of hcp crystals and red atoms belong to the liquid phase, make up dislocation cores, or surround point defects. With this coloring scheme, a single green layer and a double green layer correspond to a twin boundary and a stacking fault in the fcc structure, respectively. The resolidification process is completed by 720 ps after the laser pulse and the top 3.5 nm surface layer is blanked in all snapshots to expose the underlying defect structure in the snapshot shown for 720 ps, where the surface roughness of ~2 nm is observed.

induced melting and resolidification processes revealed in the three large-scale simulations using combined two-temperature model (TTM) and classical molecular dynamics method (MD) performed for Ni targets with (100), (011), and (111) surface orientations is similar and consists of the rapid melting of the top 21 to 24 nm surface layers of the targets followed by resolidification of the transiently melted layers. Due to the sharp temperature gradients created by the localized laser energy deposition and the fast electronic heat transfer to the bulk of the targets, the temperature of the liquid-crystal interface drops below the equilibrium melting temperature of Ni and the melting turns into solidification as early as ~50 ps after the laser pulse. The solidification proceeds through the epitaxial regrowth of the substrate and takes 400, 490, and 720 ps for complete solidification of targets with (100), (011), and (111) surface orientations, respectively. Similarly to the earlier reports for Cr and Ag targets,[16,25] the formation of vacancies at the rapidly advancing solidification fronts results in the strong vacancy supersaturation of the resolidified regions of the targets, with vacancy concentration reaching the levels of ~10^{-3} per lattice site.

One notable effect that is only observed in the course of the epitaxial resolidification of the target with (111) surface orientation is the formation of a high density of coherent twin boundaries, Σ3 {111}, at the final stage of the solidification process. This effect is illustrated in Figure 6, where a series of snapshots of atomic configurations in the top 30 nm surface layers of the Ni(111) target are shown. The initial stage of the resolidification process, from 50 to 200 ps, proceeds by the epitaxial regrowth of the crystal, as illustrated by a snapshot shown for 100 ps after the laser pulse. The solidification proceeds simultaneously with increasing undercooling of the melted layer (red region in Figure 6), the velocity of the crystal−liquid interface increases, and a large number of vacancies (red dots) are left behind the solidification front. The green ribbons outlined by red lines in the bottom part of the snapshot correspond to 1/2⟨110⟩ dislocations split into two Shockley partials (red lines) connected by stacking faults (green ribbons). These dislocations are emitted from the melting front during the dynamic relaxation of the laser-induced stresses.

The defect structure of the resolidified region changes abruptly when the temperature in the vicinity of the solidification front drops down to about 0.85T_m at about 180 ps after the laser pulse, and a large number of coherent twin boundaries appear in the planes parallel to the advancing (111) crystal−liquid interface. The twin boundaries (green layers parallel to the surface) can be seen in the snapshot shown in Figure 6 for 300 ps, and the region affected by twinning expands as the solidification front propagates toward the surface of the target. A clear view of multiple twin boundaries with a characteristic thickness of twinned domains on the order of several nm is provided in Figure 7, where the final microstructure of the top part of the resolidified target, shown without blanking the fcc atoms, and an enlarged view of a representative vertical cross-section of the surface layer are presented.

The flat islands of the coherent twin boundaries are connected with each other by incoherent twin boundary segments that remain relatively mobile after the complete solidification. One can expect that the motion of the incoherent twin boundaries would result in the disappearance of some of the smaller twinned domains upon further cooling of the surface down to the room temperature. Nevertheless, some of the twin boundaries can be expected to remain in the target as the mobility of the incoherent twin boundaries sharply drops with increasing thickness of the twinned domains.[47] To illustrate this point, the atomic configuration shown in Figure 7a has been annealed at 0.9T_m for 1.5 ns. While many of the smaller twinned domains disappear during the annealing, the final characteristic size of the twinned domains still remains at a level of ~10 nm.

DOI: 10.1021/acsnano.6b02970
ACS Nano 2016, 10, 6995−7007

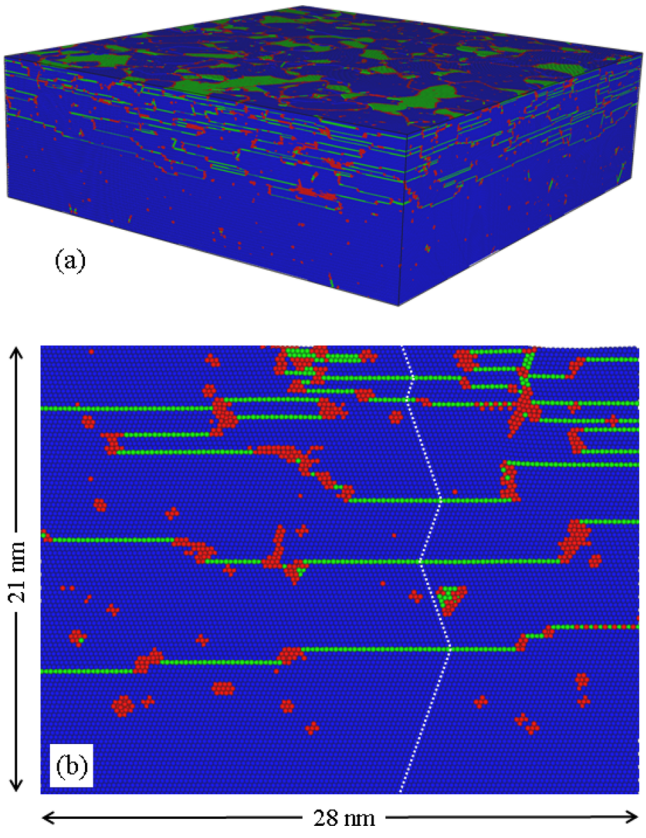

Figure 7. Alternative view of the last configuration (720 ps) of Figure 6, in which the fcc atoms are shown and colored blue (a) and an enlarged view of a representative vertical cross-section of the surface layer of the resolidified target (b). The dashed line in (b) shows the altering orientation of atomic planes in the twinned domains.

To make a direct connection to the experimental observation of twinning in the surface regions of the irradiated targets, the pole figures similar to the one shown in Figure 2b are calculated for the three targets that experienced laser melting and resolidification. The pole figures in Figure 8 show the projections of ⟨111⟩ directions for all fcc atoms in the top 20 nm surface regions of the resolidified targets, with the ⟨111⟩ poles corresponding to the original ⟨111⟩ directions in the single crystal targets marked by circles. In the pole figure calculated for the target with (111) surface orientation, new ⟨111⟩ poles created by the growth twinning are clearly present and marked by triangles in Figure 8a. In contrast, only the original ⟨111⟩ poles are present in the pole figures calculated for targets with (100) and (011) surface orientations, Figure 8b and c, indicating that no twins are introduced by laser-induced melting and resolidification of these targets. The computational predictions are in a good agreement with the experimental observation of the appearance of new poles associated with twinning for targets with (111) surface orientation, Figure 2b, and the absence of twinning in targets with (100) surface orientation.

Mechanisms of Growth Twinning under Conditions of Strong Undercooling. In order to evaluate the conditions for the formation of Σ3 {111} growth twins in the process of rapid solidification, a series or small scale simulations is performed under fixed temperature and zero pressure conditions for a 28 nm × 28 nm × 50 nm system containing, in its initial state, a 11 nm thick crystalline slab with two (111) surfaces surrounded by liquid. No twins are observed to form in the solidification process occurring under conditions of weak undercooling, at $T > 0.86T_m$. The formation of first twin boundaries is detected at $T \approx 0.86T_m$, and the density of the twin boundaries is increasing with decreasing temperature. The threshold-like condition for the onset of the generation of the growth twins and the decreasing size of the twinned domains with increasing undercooling can be explained by a simple thermodynamic model[48] that considers the advancement of the solidification front through the nucleation and lateral growth of two-dimensional atomic islands on (111) terraces of the solid–liquid interface. This model is briefly outlined and applied to the epitaxial regrowth (111) Ni targets below.

The nucleation of a new atomic layer on a (111) facet of the growing fcc crystal can produce one of the two possible stacking sequences of the close packed atomic planes, ABC sequence of the regular fcc structure and ABA sequence which, in turn, may lead to the formation of a twin boundary (ABACB sequence of planes) or a stacking fault (ABABCA or ABACAB for the intrinsic and extrinsic stacking faults, respectively) in the growing fcc crystal. Given the more than twice higher energy of the stacking faults as compared to twins[49] we can neglect the possibility of the appearance of stacking faults in the growth process and only consider the formation of twins. The change in the free energy due to the nucleation of a round atomic island of radius r with the fcc stacking sequence of the close packed planes can be expressed as

$$\Delta G_r^{fcc}(r, T) = 2\pi r\gamma_{step} - \pi r^2 h \Delta G_v(T) \quad (1)$$

where $\Delta G_v(T)$ is the free energy difference between the liquid and solid phases per unit volume (see Methods), h is the

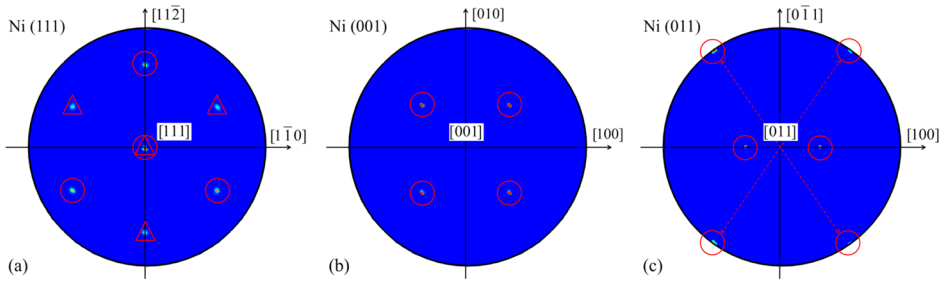

Figure 8. The ⟨111⟩ pole figures calculated for 20 nm top regions of Ni targets with (111), (100), and (011) surface orientations irradiated by 50 fs laser pulses at an absorbed fluence of 0.06 J/cm^2. All calculations are done after complete solidification of the irradiated targets. The ⟨111⟩ poles that correspond to the original single crystal are marked by circles and the new ⟨111⟩ poles generated by twinning are marked by triangles. The twinning is only observed for (111) surface orientation of the irradiated target.

DOI: 10.1021/acsnano.6b02970
ACS Nano 2016, 10, 6995–7007

spacing between {111} planes and γ_{step} is the free energy per unit length of a step on a {111} solid–liquid interface. When the nucleation results in the ABA stacking of the planes, the extra energy associated with the faulted stacking has to be accounted for in the free energy calculation and can be approximated by the energy of the twin boundary in a bulk crystal, γ_{twin}. The energy of the circular nucleus in this case can be expressed as

$$\Delta G_r^{twin}(r, T) \approx 2\pi r\gamma_{step} - \pi r^2(h\Delta G_v(T) - \gamma_{twin}) \quad (2)$$

It is apparent from the above equation that small values of undercooling, when $\Delta G_v < \gamma_{twin}/h$, the free energy is increasing for any radius of the nucleus, and no growth twins can be generated. Using the approximation of $\Delta G_v \approx \Delta H_f(1 - T/T_m)$, the critical temperature below which the twin boundaries can be formed in the solidification process can be estimated as

$$T_c \approx T_m\left(1 - \frac{\gamma_{twin}}{\Delta H_f h}\right) \quad (3)$$

For the EAM potential used in the MD simulations of Ni,[50] γ_{twin} = 68 mJ/m^2, ΔH_f = 0.187 eV/atom = 2.59 × 10^9 Jm^{-3}, h = 2.07 Å at the melting point, and the value of T_c can be estimated to be 0.87T_m. An estimation based on experimental parameters of Ni, γ_{twin} = 43 mJ/m^2,[50] ΔH_f = 2.58 × 10^9 Jm^{-3},[51] and h = 2.09 Å at $T \approx T_m$,[52] yields a comparable value of T_c = 0.92T_m.

From the free energy expressions given by eqs 1 and 2, the activation barriers for the formation of the fcc and twinned nuclei can be obtained:

$$G^*_{fcc}(T) \approx \frac{\pi\gamma_{step}^{\ 2}}{h\Delta G_v(T)}, \quad G^*_{twin}(T) \approx \frac{\pi\gamma_{step}^{\ 2}}{h\Delta G_v(T) - \gamma_{twin}} \quad (4)$$

The relative probability of the nucleation of twin and fcc planes can then be expressed as the ratio of the corresponding nucleation rates:

$$\frac{I_{twin}}{I_{fcc}} \approx \exp\left(\frac{[G^*_{fcc}(T) - G^*_{twin}(T)]\Omega_a}{k_B T}\right) \approx \exp\left(-\frac{\pi\gamma_{step}^{\ 2}\gamma_{twin}\Omega_a}{k_B T h\Delta G_v(T)[h\Delta G_v(T) - \gamma_{twin}]}\right) \quad (5)$$

This equation suggests that the nucleation of twins starts when the temperature of the crystal–liquid interface drops below T_c and the probability of the twin formation increases with increasing undercooling. These conclusions of the theoretical analysis are in a good agreement with the results of TTM-MD simulations (Figures 6 and 7), where the appearance of twin boundaries is only observed when the temperature drops below 0.85T_m and the twinning domains get thinner closer to the top surface of the target, where the solidification takes place under conditions of stronger undercooling.

Laser Fluence Dependence of the Solidification Conditions and Twinning. To predict the dependence of the thickness of the surface layer affected by the growth twinning on laser fluence, a series of continuum-level simulations are performed with the TTM model enhanced with a description of nonequilibrium melting and solidification as explained in Methods. The simulations are performed for the values of absorbed laser fluence ranging from 0.05 J/cm^2, just above the threshold for surface melting, up to 0.13 J/cm^2, close to the threshold for photomechanical spallation identified in TTM-MD simulations.

The results of the simulations are shown in Figure 9, where the evolution of the melting depth and temperature at the liquid–crystal interface are plotted for different laser fluences. The fast homogeneous melting, occurring on the time-scale of electron–phonon equilibration, is responsible for the initial jump of the melting depth and is followed by additional heterogeneous melting through the propagation of the melting front deeper into the bulk of the target at higher fluences. The melting is followed by resolidification of the target proceeding under conditions of increasing undercooling of the liquid–crystal interface below the equilibrium melting temperature. The fastest cooling and the maximum undercooling at the end of the resolidification process are realized close to the melting threshold, when the melting depth is comparable to the depth of the laser energy deposition and a steep temperature gradient is created at the liquid–crystal interface by the end of the homogeneous melting process. The cooling rate and the maximum undercooling are decreasing with increasing fluence, with the temperature of the liquid–crystal interface at the time it reaches the surface raising from its minimum of ~0.58T_m at 0.06 J/cm^2 up to ~0.74T_m at 0.13 J/cm^2. The overall picture of the fluence dependence of the melting and resolidification processes predicted in the TTM calculations is consistent with the earlier TTM-MD simulations performed for Ni targets,[23] with small quantitative differences related to the differences in the parameters adopted in the two series of simulations.

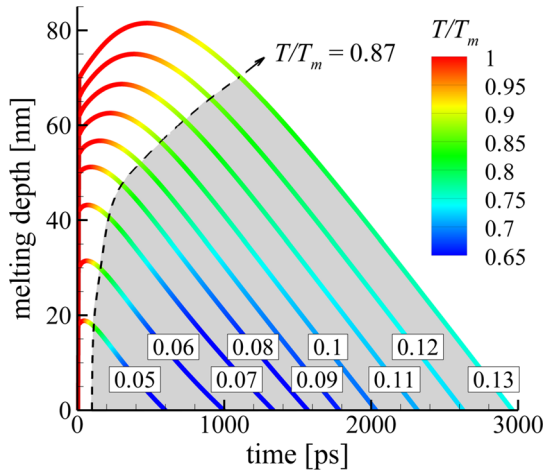

Figure 9. Evolution of the melting depth and temperature at the liquid–crystal interface predicted in TTM calculations accounting for the kinetics of nonequilibrium meting/solidification. The curves on the plot correspond to simulations of Ni targets irradiated by a 50 fs laser pulse at different values of absorbed laser fluence marked in the plot in units of J/cm^2. The lines are colored according to the temperature at the solidification front. The gray region outlined by the dashed line corresponds to the conditions of strong undercooling (T < 0.87 T_m), when the growth twinning is predicted in the theoretical analysis and atomistic TTM-MD simulations.

The condition for the onset of growth twinning, T = 0.87T_m, predicted theoretically and confirmed in the atomistic simulations, is marked in Figure 9 by the dashed line. The depth of the region affected by twinning (gray region in Figure 9) increases rapidly at laser fluences close to the melting threshold and shows signs of saturation as the laser fluence

DOI: 10.1021/acsnano.6b02970
ACS Nano 2016, 10, 6995–7007

approaches the spallation threshold. Note that the decrease of the cooling rate and the levels of undercooling with increasing fluence suggest that the depth of the surface region affected by twinning may even shrink at higher laser fluences in materials with higher energies of twin boundaries, where T_c is lower, eq 3. Moreover, the weaker undercooling can be expected to result in the lower probability of the nucleation of twin boundaries, eq 5, thus increasing the average thickness of twinned domains at higher laser fluences.

The computational results provide an explanation for the increase of both the region affected by twinning and the thickness of twinned domains with increasing laser fluence observed in experiments discussed earlier. Using reflectivity of 0.7 at laser wavelength of 800 nm,[45] the experimental incident laser fluences of 0.19 and 0.38 J/cm^2 can be converted to absorbed fluences of 0.057 and 0.114 J/cm^2, respectively. The TTM calculations predict the maximum levels of undercooling at the end of resolidification of $0.58T_m$ and $0.71T_m$ at the absorbed fluences of 0.06 and 0.11 J/cm^2, respectively, thus explaining the substantially larger thickness of the twined domains observed at the higher laser fluence. Moreover, the region affected by the growth twinning is predicted to be deeper at the higher fluence, which is also qualitatively consistent with the experimental observations; see Figures 4e and 5b.

Further increase of the laser fluence beyond the spallation/ablation threshold results in removal of a hot surface material from the bulk target, leading to the increase in the cooling rate during the solidification of the remaining shallow melted region.[23] The two factors, namely, the drop in the depth of the melted region remaining after the ablation of the top layer of the target and the increase in the cooling rate, compete with each other in defining the final thickness of the twinned region. The evaluation of the dependence of the layer affected by growth twinning on laser fluence in the ablation regime is ongoing and will be reported elsewhere. Irradiation with longer laser pulses, in the range of hundreds of picoseconds and nanoseconds, produces smaller temperature gradients and cooling rates during resolidification,[53] and reduces the depth of the twinned region. Continuum level TTM calculations suggest that pulses longer than 3 ns cannot produce a sufficiently strong undercooling for generation of growth twins in Ni(111) targets.

Connections between Transient Phase Transformations and Generation of HSFL. The clear experimental evidence of the laser-induced generation of a laminar subsurface structure composed of twinned domains and epilayers, combined with the mechanistic insights provided by the theoretical analysis and atomistic simulations, indicates that the growth twinning can be used as a sensitive "fingerprint" of the transient melting and resolidification induced in a fcc metal target/grain with {111} surface orientation by short pulse laser irradiation at laser fluences near the melting threshold. In the absence of growth twinning, the structural signatures of the transient melting and resolidification (*e.g.*, generation of a high vacancy concentration in a Cr(001) target[16]) may be too weak to be detected in *ex situ* experimental characterization. The results of the atomistic simulations performed for Ni targets with three low-index surface orientations also suggest that melting followed by the epitaxial resolidification produces relatively small surface roughness on the order of 1−2 nm, which is comparable to the roughness of polished surface before the irradiation (see Methods). We can conclude, therefore, that the growth twinning in fcc metal targets with {111} surface orientation provides the most clear marker of melting at laser fluences below the threshold for subsurface cavitation and spallation.[17,23]

The generation of the subsurface twins in the irradiated Ni(111) targets correlates with the formation of HSFL in the multipulse irradiation regime: The HSFL are observed exclusively in the central part of the laser spot, where the subsurface twins are also present, suggesting a direct link between the transient melting and the formation of the HSFL. Despite the relatively small thickness of the layer experiencing laser melting and resolidification (the total thickness of the twinned domains and epilayers at the center of the laser spot measures about 30 nm), the HSFL with sub-100 nm periodicity are observed to grow entirely in the resolidified layer, with the peak-to-valley amplitude attaining 20 nm in the center, Figure 3. This observation suggests a substantial redistribution of the melted material in the course of repetitive laser melting and resolidification of the thin surface layer of the target. While the exact mechanisms driving the material redistribution remain the subjects of ongoing debates,[29,33−40] the results of the present study suggest an important role of the laser-induced surface melting in the formation of HSFL. The presence of a twinned domain in the off-center part of the laser spot (Figure 5a), where no HSFL is observed, also suggests that the development of the surface roughness may rely on the melting depth exceeding a certain minimum level.

Note that HSFL shown in Figures 1 and 3 are formed at a laser fluence that is substantially below the spallation/ablation threshold, and generation of HSFL is not related to the material removal from the irradiated target. Moreover, notwithstanding the appearance of several burst nanobubbles on the highest ridges in Figure 1, the cross-sectional examination of the samples does not reveal any noticeable signs of nanoscale cavitation instability[39,40] or generation of subsurface voids.[17] Furthermore, the experimental characterization suggests a negligible amount of oxygen present at laser-irradiated Ni surface. Therefore, in contrast to titanium or other metals where localized surface oxidation could induce topography changes and/or higher harmonic generation, hence enhancing absorption and contributing to HSFL formation,[37,54] neither oxides nor amorphous phase were discerned throughout our high resolution cross-sectional study. Thus, surface oxidation upon femtosecond laser irradiation is unlikely to cause HSFL formation on Ni surface irradiated at moderate laser fluences. Overall, the results of experimental characterization of laser-processed targets, combined with predictions of atomistic and continuum-level simulations, provide a clear evidence of an intrinsic link between the laser-induced melting and HSFL formation. The exact interplay between the melting, hydrodynamic motion of the melt, and the emergence of HSFL upon repetitive laser irradiation, however, still remains to be explored in future studies.

CONCLUSIONS

The results of a combined experimental and computational study of the short pulse laser interaction with single crystal Ni targets reveal a direct connection between the laser-induced melting/resolidification and the formation of HSFL. The occurrence of melting is evidenced by the formation of nanoscale lamellar structures of interlaying twinned domains and epilayers in the surface regions of irradiated Ni(111) targets. Atomistic- and continuum-level simulations performed

DOI: 10.1021/acsnano.6b02970
ACS Nano 2016, 10, 6995−7007

for the experimental irradiation conditions reproduce the generation of twinned domains in the course of the rapid solidification of the transiently melted surface regions of the irradiated targets. Theoretical analysis of the microscopic mechanisms of the solidification process yields the condition leading to the onset of the growth twinning and establishes the connection between the degree of undercooling and the density of twins generated at the solidification front. The laser fluence dependence of the density and thickness of the twinned domains revealed in the experimental study is explained based on the results of continuum-level simulations of nonequilibrium laser-induced melting and resolidification. In multipulse irradiation regime, the appearance and growth of sub-100 nm HSFL oriented parallel to the laser polarization is observed in the thick twinned domains in the center of the laser spot, highlighting the connections between melting, melt depth, and generation of HSFL.

METHODS

Materials and Laser Irradiation. The experimental study is focused on microstructural analysis of single crystal Ni targets irradiated by femtosecond laser pulses at different fluences. In order to highlight HSFL features, low fluence and large number of laser pulses were applied. The fluence dependence of the subsurface microstructure is explored by performing an additional series of experiments at a higher laser fluence and smaller number of pulses. Nickel single-crystal targets were prepared by conventional metallographic procedures with a final surface roughness average R_a = 1 nm. The HSFL on the surfaces of Ni targets were produced using a Ti:Sapphire femtosecond laser system (Legend Coherent Inc.). The laser has a central wavelength of 800 nm with a pulse duration of 50 fs and a repetition rate of 1 kHz. The linearly polarized laser pulses were attenuated and focused through a 250 mm achromatic lens at a normal incidence angle. The focused laser spot exhibits a Gaussian profile and the spot size (at $1/e^2$) measures $2w_0$ = 52 μm. The laser fluence quoted in this paper is the peak fluence $F = 2E/\pi w_0^2$, with E being the laser pulse energy. The single shot ablation threshold of 0.39 J/cm^2 was determined by the D^2 method.[55]

Microscopy. The analysis of surface modifications in the laser impact area was performed using a scanning electron microscope (Zeiss Supra55 FEG-SEM), equipped with an EBSD system from HKL-Oxford Instruments. The surface topography was measured by using an atomic force microscope (Agilent 5500). Detailed description of the experimental conditions can be found in our previous paper.[31] Microstructural examination in the direction normal to the surface (*i.e.*, from the surface to subsurface to bulk) was carried out using a field emission high-resolution transmission electron microscope (JEOL 2010F) system on cross section lamellae extracted from laser irradiated sites. TEM lamella preparation was performed using a FIB/SEM workstation (NVision 40; Carl Zeiss Microscopy GmbH, Oberkochen, Germany) combining a SIINT zeta FIB column (Seiko Instruments Inc. NanoTechnology, Japan) with a Gemini I column. The NVision 40 platform is equipped with a multinozzle SIINT Gas Injection System (GIS). The *in situ* lift-out of the thin foils from preselected sections of the laser irradiated site was carried out with a Cartesian nanorobotic manipulator (Klocke Nanotechnik GmbH, Aachen, Germany). Precautions were taken during the preparation to minimize the curtain effect and surface implantation.[56] Careful milling and low kV ion polishing were applied to obtain the final TEM lamellae (thickness around 100 nm).

TTM-MD Model. The large-scale atomistic simulations of laser interactions with bulk Ni targets are performed with a hybrid atomistic–continuum model,[57] which combines the classical MD method for simulation of nonequilibrium processes of lattice superheating and fast phase transformations with the TTM[18] providing a continuum-level description of the laser excitation and subsequent relaxation of the conduction band electrons. A complete description of the TTM-MD model is provided elsewhere.[57,58] Below we only outline the computational setup used in the simulations reported in this paper.

The TTM-MD simulations are performed for single crystal Ni targets with three surface orientations, (100), (011), and (111). The atomistic parts of the TTM-MD model consist of 162, 153, and 150 million atoms for (100), (011), and (111) targets, respectively, and represent the top 150 nm surface layers of the targets, where the laser-induced structural and phase transformations (melting and resolidification) take place. In the lateral directions, parallel to the surfaces of the targets, the dimensions of the computational systems are about 100 nm × 100 nm and periodic boundary conditions are applied. In the continuum part of the model, beyond the surface layer represented with the atomic resolution, the conventional TTM equations, accounting for the electronic heat conduction and the energy exchange between the electrons and the lattice, are solved down to 2.5 μm to ensure negligible temperature changes at the bottom of the computational domain during the time of the simulations. At the bottom of the atomistic part of the model, a pressure-transmitting, heat-conducting boundary condition is applied to ensure nonreflecting propagation of the laser-induced stress wave and heat transfer from the atomistic part of the computational system into the bulk of the target.

The interatomic interaction between Ni atoms in the atomistic part of the model is described by the EAM potential, using the functional form and parametrization suggested in ref 50. The potential is fitted to the experimental values of the lattice parameter, cohesive energy, elastic constants, and vacancy formation and migration energies. The potential also provides a relatively accurate description of other material properties that are relevant to the laser-induced structural and phase transformations investigated in the present study. In particular, the equilibrium melting temperature, T_m, determined in liquid-crystal coexistence MD simulations is 1701 K,[59] only 1.6% below the experimental value of 1728 K.[51] The potential provides a more accurate, with respect to other potentials available for Ni,[50,60] description of the interfacial energies, including the energies of stacking faults, twin boundaries, and free surfaces. For example, the predicted energies of the intrinsic stacking fault and symmetrical twin boundary are 134 and 68 mJ/m^2, respectively, and compare reasonably well with the experimental counterparts of 125 and 43 mJ/m^2.[50] The surface energies are predicted to be 2087, 1936, and 1759 mJ/m^2 for the (011), (100), and (111) surfaces, respectively, and are relatively close to the experimental value of 2280 mJ/m^2, average over surface orientations.[61]

The irradiation of the target by a 50 fs laser pulse is represented through a source term added to the TTM equation for the electron temperature.[57] The source term simulates the excitation of the conduction band electrons by a laser pulse with a Gaussian temporal profile and reproduces the exponential attenuation of laser intensity with depth under the surface (Beer–Lambert law), with the optical absorption depth of 14.5 nm assumed for Ni at the laser wavelength of 800 nm.[62] The uniform laser energy deposition is applied along the lateral directions, and the absorbed laser fluence in all TTM-MD simulations is chosen to be 0.06 J/cm^2. Assuming the reflectivity of 0.7,[45] this absorbed fluence corresponds to the incident fluence of 0.20 J/cm^2, which is very close to the incident peak fluence of 0.19 J/cm^2 used in the experiments.

The electron temperature dependences of the electron–phonon coupling factor and the electron heat capacity used in the TTM equation for the electron temperature are taken in the forms that account for the contribution from the thermal excitation from the electron states below the Fermi level.[63,64] The temperature dependence of the electron thermal conductivity is approximated by the Drude model relationship, $K_e(T_e, T_l) = \nu^2 C_e(T_e)\,\tau_e(T_e, T_l)/3$, where $C_e(T_e)$ is the electron heat capacity, ν^2 is the mean square velocity of the electrons contributing to the electron heat conductivity, approximated in this work as the Fermi velocity squared, v_F^2, and $\tau_e(T_e, T_l)$ is the total electron scattering time defined by the electron–electron scattering rate, $1/\tau_{e-e} = AT_e^2$, and the electron–phonon scattering rate, $1/\tau_{e-ph} = BT_l$, so that $1/\tau_e = AT_e^2 + BT_l$. The value of the coefficient A (1.40×10^6 K^{-2} s^{-1}) is estimated within the free electron model.[65] The coefficient B is described as a function of the

DOI: 10.1021/acsnano.6b02970
ACS Nano 2016, 10, 6995–7007

lattice temperature and the materials phase state, so that the experimental temperature dependences of thermal conductivity of the solid and liquid Ni under conditions of electron−phonon equilibrium[66] are reproduced in the simulations.

TTM Model with Nonequilibrium Melting and Solidification. The data on the kinetics of melting and resolidification processes and the conditions for the onset of growth twinning obtained in the atomistic simulations are incorporated into the conventional TTM model adopted for a quick evaluation of the laser fluence dependence of the thickness of the surface layer affected by the growth twinning. The equations of TTM model are solved using the backward (implicit) Euler algorithm based on block tridiagonal matrix inversion. The material parameters in the TTM equation for the electron temperature are the same as in the TTM-MD model described above. The lattice heat conduction is neglected and the lattice heat capacity is assumed to be constant and equal to 3.96×10^6 Jm^{-3} K^{-1}.[51]

The motion of the solid−liquid interface is described by the following equations:

$$\frac{dX_I}{dt} = V_I(T_I) = \int_0^L V_I(T(x, t))\, f(x)\, dx \tag{6}$$

$$S_I = V_I(T_I)\, \Delta H_f f(x - X_I) \tag{7}$$

$$f(x) = \frac{1}{\sqrt{2\pi\sigma^2}} \exp\left(-\frac{x^2}{2\sigma^2}\right) \tag{8}$$

where X_I is the position of the solid−liquid interface, V_I is the velocity of the interface, T_I is the lattice temperature at the interface, L is the size of the computational system used in eq 6 to ensure that the interface is covered by the integration, ΔH_f is the heat of fusion of the target material, S_I is the energy source term added to the TTM equation for the lattice temperature to account for the heat released or absorbed due to movement of the solid−liquid interface, $f(x)$ is the Gaussian function that approximates the Dirac delta function defining the position of the interface, and σ is the thickness of the interface taken to be 2 nm.

The temperature dependence of the velocity of the liquid−crystal interface is described by the Wilson−Frenkel expression:[67]

$$V_I = V_0 \exp(-Q\Omega_a/k_BT)[1 - \exp(-\Delta G_v(T)\Omega_a/k_BT)] \tag{9}$$

where V_0 is a prefactor, Q is the activation energy per unit volume, $\Delta G_v = G_v^l - G_v^s$ is the free energy difference between the liquid and solid phases per unit volume, Ω_a is the atomic volume of the solid phase at the equilibrium melting temperature T_m, and k_B is the Boltzmann constant. The value of ΔG_v is approximated as $\Delta G_v \approx \Delta H_f(1 - T/T_m)$, with experimental values of $T_m = 1728$ K and $\Delta H_f = 2.58 \times 10^9$ J/m^3 used for Ni.[51] It has been shown that eq 9 provides an adequate description of the velocity of crystallization front in fcc metals down to $\sim 0.6T_m$,[68,69] *i.e.*, in the range of temperatures realized in the simulations of laser melting and resolidification.[17,23] The values of parameters $V_0 = 2270$ m/s and $Q = 4.52 \times 10^9$ J/m^3 (correspond to 0.326 eV/atom with $\Omega_a = 11.55$ Å^3 obtained from MD simulations) are calculated by fitting eq 9 to the velocities predicted for (111) Ni interface in MD simulations performed under controlled temperature and pressure conditions in the range of temperatures from $0.65T_m$ to $0.95T_m$. To account for the fast homogeneous melting of crystals superheated above $\sim 1.2T_m$,[70,71] the regions of the target where the lattice temperature exceeds $1.2T_m$ are set to undergo instantaneous melting.

AUTHOR INFORMATION

Corresponding Author

*E-mail: jean.philippe.colombier@univ-st-etienne.fr.

Author Contributions

⊥X.S. and M.V.S. contributed equally to this work.

Notes

The authors declare no competing financial interest.

ACKNOWLEDGMENTS

Experimental part of the work was supported by LABEX MANUTECH-SISE (ANR-10-LABX-0075) of Université de Lyon, within program "Investissements d'Avenir" (ANR-11-IDEX-0007). Computational and theoretical parts are supported by the National Science Foundation (NSF) through Grants CMMI-1301298 and CMMI-1436775. Computational resources were provided by NSF through the Extreme Science and Engineering Discovery Environment (Project TG-DMR110090). The access to the JEOL2010F microscope and the Zeiss NVision40 FIB/SEM was provided by the CLYM (Centre Lyonnais de Microscopie: www.clym.fr) supported by the CNRS, the "GrandLyon" and the Rhône-Alpes Region.

REFERENCES

(1) Ahmmed, K. M. T.; Grambow, C.; Kietzig, A.-M. Fabrication of Micro/Nano Structures on Metals by Femtosecond Laser Micromachining. *Micromachines* **2014**, *5*, 1219−1253.

(2) Kononenko, T. V.; Garnov, S. V.; Klimentov, S. M.; Konov, V. I.; Loubnin, E. N.; Dausinger, F.; Raiber, A.; Taut, C. Laser Ablation of Metals and Ceramics in Picosecond−nanosecond Pulsewidth in the Presence of Different Ambient Atmospheres. *Appl. Surf. Sci.* **1997**, *109−110*, 48−51.

(3) Chichkov, B. N.; Momma, C.; Nolte, S.; von Alvensleben, F.; Tünnermann, A. Femtosecond, Picosecond and Nanosecond Laser Ablation of Solids. *Appl. Phys. A: Mater. Sci. Process.* **1996**, *63*, 109−115.

(4) Cunha, A.; Serro, A. P.; Oliveira, V.; Almeida, A.; Vilar, R.; Durrieu, M.-C. Wetting Behaviour of Femtosecond Laser Textured Ti−6Al−4V Surfaces. *Appl. Surf. Sci.* **2013**, *265*, 688−696.

(5) Vorobyev, A. Y.; Guo, C. Colorizing Metals with Femtosecond Laser Pulses. *Appl. Phys. Lett.* **2008**, *92*, 041914.

(6) Bazaka, K.; Crawford, R. J.; Ivanova, E. P. Do Bacteria Differentiate between Degrees of Nanoscale Surface Roughness? *Biotechnol. J.* **2011**, *6*, 1103−1114.

(7) Gnilitskyi, I.; Pavlov, I.; Rotundo, F.; Orazi, L.; Martini, C.; Ilday, F. Ö. Nonlinear Laser Lithography for Enhanced Tribological Properties. In *CLEO: 2015, OSA Technical Digest (online)*; Optical Society of America: Washington, DC, 2015; paper AM2K.2.

(8) Orazi, L.; Liverani, E.; Ascari, A.; Fortunato, A.; Tomesani, L. Laser Surface Hardening of Large Cylindrical Components Utilizing Ring Spot Geometry. *CIRP Ann.* **2014**, *63*, 233−236.

(9) Hou, S.; Huo, Y.; Xiong, P.; Zhang, Y.; Zhang, S.; Jia, T.; Sun, Z.; Qiu, J.; Xu, Z. Formation of Long- and Short-Periodic Nanoripples on Stainless Steel Irradiated by Femtosecond Laser Pulses. *J. Phys. D: Appl. Phys.* **2011**, *44*, 505401−505407.

(10) Mannion, P. T.; Magee, J.; Coyne, E.; O'Connor, G. M.; Glynn, T. J. The Effect of Damage Accumulation Behaviour on Ablation Thresholds and Damage Morphology in Ultrafast Laser Micro-Machining of Common Metals in Air. *Appl. Surf. Sci.* **2004**, *233*, 275−287.

(11) Raciukaitis, G.; Brikas, M.; Gecys, P.; Gedvilas, M. Accumulation Effects in Laser Ablation of Metals with High-Repetition-Rate Lasers. *Proc. SPIE* **2008**, *7005*, 70052L.

(12) Byskov-Nielsen, J.; Savolainen, J.-M.; Christensen, M.; Balling, P. Ultra-Short Pulse Laser Ablation of Metals: Threshold Fluence, Incubation Coefficient and Ablation Rates. *Appl. Phys. A: Mater. Sci. Process.* **2010**, *101*, 97−101.

(13) Jee, Y.; Becker, M. F.; Walser, R. M. Laser-Induced Damage on Single-Crystal Metal Surfaces. *J. Opt. Soc. Am. B* **1988**, *5*, 648−659.

(14) Koumvakalis, N.; Lee, C. S.; Bass, M. Single and Multiple Pulse Catastrophic Damage in Diamond-Turned Cu and Ag Mirrors at 10.6, 1.06, and 0.532 μm. *Opt. Eng.* **1983**, *22*, 419−423.

(15) Thomas, S. J.; Harrison, R. F.; Figueira, J. F. Observations of the Morphology of Laser-Induced Damage in Copper Mirrors. *Appl. Phys. Lett.* **1982**, *40*, 200−202.

DOI: 10.1021/acsnano.6b02970
ACS Nano 2016, 10, 6995−7007

(16) Lin, Z.; Johnson, R. A.; Zhigilei, L. V. Computational Study of the Generation of Crystal Defects in a Bcc Metal Target Irradiated by Short Laser Pulses. *Phys. Rev. B: Condens. Matter Mater. Phys.* **2008**, *77*, 214108.
(17) Wu, C.; Christensen, M. S.; Savolainen, J.-M.; Balling, P.; Zhigilei, L. V. Generation of Subsurface Voids and a Nanocrystalline Surface Layer in Femtosecond Laser Irradiation of a Single-Crystal Ag Target. *Phys. Rev. B: Condens. Matter Mater. Phys.* **2015**, *91*, 035413.
(18) Anisimov, S. I.; Kapeliovich, B. L.; Perel'man, T. L. Electron Emission from Metal Surfaces Exposed to Ultrashort Laser Pulses. *J. Exp. Theor. Phys.* **1974**, *39*, 375−377.
(19) Colombier, J.-P.; Garrelie, F.; Faure, N.; Reynaud, S.; Bounhalli, M.; Audouard, E.; Stoian, R.; Pigeon, F. Effects of Electron-Phonon Coupling and Electron Diffusion on Ripples Growth on Ultrafast-Laser-Irradiated Metals. *J. Appl. Phys.* **2012**, *111*, 024902.
(20) Colombier, J.-P.; Garrelie, F.; Brunet, P.; Bruyère, A.; Pigeon, F.; Stoian, R.; Parriaux, O. Plasmonic and Hydrodynamic Effects in Ultrafast Laser-Induced Periodic Surface Structures on Metals. *J. Laser Micro/Nanoeng.* **2012**, *7*, 362−368.
(21) Tsibidis, G. D.; Barberoglou, M.; Loukakos, P. A.; Stratakis, E.; Fotakis, C. Dynamics of Ripple Formation on Silicon Surfaces by Ultrashort Laser Pulses in Sub-Ablation Conditions. *Phys. Rev. B: Condens. Matter Mater. Phys.* **2012**, *86*, 115316.
(22) Tsibidis, G. D.; Fotakis, C.; Stratakis, E. From Ripples to Spikes: A Hydrodynamical Mechanism to Interpret Femtosecond Laser-Induced Self-Assembled Structures. *Phys. Rev. B: Condens. Matter Mater. Phys.* **2015**, *92*, 041405.
(23) Zhigilei, L. V.; Lin, Z.; Ivanov, D. S. Atomistic Modeling of Short Pulse Laser Ablation of Metals: Connections between Melting, Spallation, and Phase Explosion. *J. Phys. Chem. C* **2009**, *113*, 11892−11906.
(24) Wu, C.; Karim, E. T.; Volkov, A. N.; Zhigilei, L. V. Atomic Movies of Laser-Induced Structural and Phase Transformations from Molecular Dynamics Simulations. In *Lasers in Materials Science*; Castillejo, M., Ossi, P. M., Zhigilei, L., Eds.; Springer Series in Materials Science Vol. *191*; Springer International Publishing: Cham, Switzerland, 2014; pp 67−100.
(25) Karim, E. T.; Wu, C.; Zhigilei, L. V. Molecular Dynamics Simulations of Laser-Materials Interactions: General and Material-Specific Mechanisms of Material Removal and Generation of Crystal Defects. In *Fundamentals of Laser-Assisted Micro- and Nanotechnologies*; Veiko, V. P., Konov, V. I., Eds.; Springer Series in Materials Science Vol. *195*; Springer International Publishing: Cham, Switzerland, 2014; pp 27−49.
(26) Wu, C.; Zhigilei, L. V. Nanocrystalline and Polyicosahedral Structure of a Nanospike Generated on Metal Surface Irradiated by a Single Femtosecond Laser Pulse. *J. Phys. Chem. C* **2016**, *120*, 4438−4447.
(27) Sipe, J. E.; Young, J. F.; Preston, J. S.; van Driel, H. M. Laser-Induced Periodic Surface Structure. I. Theory. *Phys. Rev. B: Condens. Matter Mater. Phys.* **1983**, *27*, 1141−1154.
(28) Garrelie, F.; Colombier, J. P.; Pigeon, F.; Tonchev, S.; Faure, N.; Bounhalli, M.; Reynaud, S.; Parriaux, O. Evidence of Surface Plasmon Resonance in Ultrafast Laser-Induced Ripples. *Opt. Express* **2011**, *19*, 9035−9043.
(29) Zhang, H.; Colombier, J.-P.; Li, C.; Faure, N.; Cheng, G.; Stoian, R. Coherence in Ultrafast Laser-Induced Periodic Surface Structures. *Phys. Rev. B: Condens. Matter Mater. Phys.* **2015**, *92*, 174109.
(30) Huang, M.; Zhao, F.; Cheng, Y.; Xu, N.; Xu, Z. Origin of Laser-Induced Near-Subwavelength Ripples: Interference between Surface Plasmons and Incident Laser. *ACS Nano* **2009**, *3*, 4062−4070.
(31) Sedao, X.; Maurice, C.; Garrelie, F.; Colombier, J.-P.; Reynaud, S.; Quey, R.; Blanc, G.; Pigeon, F. Electron Backscatter Diffraction Characterization of Laser-Induced Periodic Surface Structures on Nickel Surface. *Appl. Surf. Sci.* **2014**, *302*, 114−117.
(32) Sedao, X.; Maurice, C.; Garrelie, F.; Colombier, J.-P.; Reynaud, S.; Quey, R.; Pigeon, F. Influence of Crystal Orientation on the Formation of Femtosecond Laser-Induced Periodic Surface Structures and Lattice Defects Accumulation. *Appl. Phys. Lett.* **2014**, *104*, 171605.
(33) Nathala, C. S. R.; Ajami, A.; Ionin, A. A.; Kudryashov, S. I.; Makarov, S. V.; Ganz, T.; Assion, A.; Husinsky, W. Experimental Study of fs-Laser Induced Sub-100-nm Periodic Surface Structures on Titanium. *Opt. Express* **2015**, *23*, 5915−5929.
(34) Bonse, J.; Krüger, J.; Höhm, S.; Rosenfeld, A. Femtosecond Laser-Induced Periodic Surface Structures. *J. Laser Appl.* **2012**, *24*, 042006.
(35) Sakabe, S.; Hashida, M.; Tokita, S.; Namba, S.; Okamuro, K. Mechanism for Self-Formation of Periodic Grating Structures on a Metal Surface by a Femtosecond Laser Pulse. *Phys. Rev. B: Condens. Matter Mater. Phys.* **2009**, *79*, 033409.
(36) Hashida, M.; Miyasaka, Y.; Ikuta, Y.; Tokita, S.; Sakabe, S. Crystal Structures on a Copper Thin Film with a Surface of Periodic Self-Organized Nanostructures Induced by Femtosecond Laser Pulses. *Phys. Rev. B: Condens. Matter Mater. Phys.* **2011**, *83*, 235413.
(37) Li, X.-F.; Zhang, C.-Y.; Li, H.; Dai, Q.-F.; Lan, S.; Tie, S.-L. Formation of 100-nm Periodic Structures on a Titanium Surface by Exploiting the Oxidation and Third Harmonic Generation Induced by Femtosecond Laser Pulses. *Opt. Express* **2014**, *22*, 28086−28099.
(38) Reif, J.; Costache, F.; Varlamova, O.; Jia, G.; Ratzke, M. Self-Organized Regular Surface Patterning by Pulsed Laser Ablation. *Phys. Status Solidi C* **2009**, *6*, 681−686.
(39) Ionin, A. A.; Kudryashov, S. I.; Ligachev, A. E.; Makarov, S. V.; Seleznev, L. V.; Sinitsyn, D. V. Nanoscale Cavitation Instability of the Surface Melt along the Grooves of One-Dimensional Nanorelief Gratings on an Aluminum Surface. *JETP Lett.* **2011**, *94*, 266−269.
(40) Ionin, A. A.; Kudryashov, S. I.; Makarov, S. V.; Seleznev, L. V.; Sinitsyn, D. V.; Ligachev, A. E.; Golosov, E. V.; Kolobov, Y. R. Sub-100 Nanometer Transverse Gratings Written by Femtosecond Laser Pulses on a Titanium Surface. *Laser Phys. Lett.* **2013**, *10*, 056004.
(41) Agranat, M. B.; Ashitkov, S. I.; Fortov, V. E.; Kirillin, A. V.; Kostanovskii, A. V.; Anisimov, S. I.; Kondratenko, P. S. Use of Optical Anisotropy for Study of Ultrafast Phase Transformations at Solid Surfaces. *Appl. Phys. A: Mater. Sci. Process.* **1999**, *69*, 637−640.
(42) Chan, W.-L.; Averback, R. S.; Cahill, D. G.; Ashkenazy, Y. Solidification Velocities in Deeply Undercooled Silver. *Phys. Rev. Lett.* **2009**, *102*, 095701.
(43) Chen, S. C.; Cahill, D. G.; Grigoropoulos, C. P. Melting and Surface Deformation in Pulsed Laser Surface Micromodification of Ni-P Disks. *J. Heat Transfer* **2000**, *122*, 107−112.
(44) Chen, J.; Chen, W.-K.; Tang, J.; Rentzepis, P. M. Time-Resolved Structural Dynamics of Thin Metal Films Heated with Femtosecond Optical Pulses. *Proc. Natl. Acad. Sci. U. S. A.* **2011**, *108*, 18887−18892.
(45) Bäuerle, D. W. *Laser Processing and Chemistry*; Springer Science & Business Media: Berlin, 2013.
(46) Vincenc Oboňa, J.; Ocelík, V.; Rao, J. C.; Skolski, J. Z. P.; Römer, G. R. B. E.; Huis in 't Veld, A. J.; De Hosson, J. Th. M. Modification of Cu Surface with Picosecond Laser Pulses. *Appl. Surf. Sci.* **2014**, *303*, 118−124.
(47) Wang, J.; Li, N.; Anderoglu, O.; Zhang, X.; Misra, A.; Huang, J. Y.; Hirth, J. P. Detwinning Mechanisms for Growth Twins in Face-Centered Cubic Metals. *Acta Mater.* **2010**, *58*, 2262−2270.
(48) Han, K.; Hirth, J. P.; Embury, J. D. Modeling the Formation of Twins and Stacking Faults in the Ag-Cu System. *Acta Mater.* **2001**, *49*, 1537−1540.
(49) Howe, J. M. *Interfaces in Materials: Atomic Structure, Thermodynamics and Kinetics of Solid-Vapor, Solid-Liquid and Solid-Solid Interfaces*; John Wiley & Sons Inc: New York, 1997.
(50) Mishin, Y. Atomistic Modeling of the γ and γ'-Phases of the Ni−Al System. *Acta Mater.* **2004**, *52*, 1451−1467.
(51) Lide, D. R. *CRC Handbook of Chemistry and Physics*, 85th ed.; CRC Press: Boca Raton, FL, 2004.
(52) Touloukian, Y. S.; Kirby, R. K.; Taylor, R. E.; Desai, P. D. *Thermophysical Properties of Matter - the TPRC Data Series. Vol. 12. Thermal Expansion Metallic Elements and Alloys*; IFI/Plenum: New York, 1975.

DOI: 10.1021/acsnano.6b02970
ACS Nano 2016, 10, 6995−7007

(53) Duff, W. H.; Zhigilei, L. V. Computational Study of Cooling Rates and Recrystallization Kinetics in Short Pulse Laser Quenching of Metal Targets. *J. Phys.: Conf. Ser.* **2007**, *59*, 413−417.
(54) Öktem, B.; Pavlov, I.; Ilday, S.; Kalaycıoğlu, H.; Rybak, A.; Yavaş, S.; Erdoğan, M.; Ilday, F. Ö. Nonlinear Laser Lithography for Indefinitely Large-Area Nanostructuring with Femtosecond Pulses. *Nat. Photonics* **2013**, *7*, 897−901.
(55) Liu, J. M. Simple Technique for Measurements of Pulsed Gaussian-Beam Spot Sizes. *Opt. Lett.* **1982**, *7*, 196−198.
(56) Ishitani, T.; Umemura, K.; Ohnishi, T.; Yaguchi, T.; Kamino, T. Improvements in Performance of Focused Ion Beam Cross-Sectioning: Aspects of Ion-Sample Interaction. *J. Electron Microsc.* **2004**, *53*, 443−449.
(57) Ivanov, D. S.; Zhigilei, L. V. Combined Atomistic-Continuum Modeling of Short-Pulse Laser Melting and Disintegration of Metal Films. *Phys. Rev. B: Condens. Matter Mater. Phys.* **2003**, *68*, 064114.
(58) Wu, C.; Zhigilei, L. V. Microscopic Mechanisms of Laser Spallation and Ablation of Metal Targets from Large-Scale Molecular Dynamics Simulations. *Appl. Phys. A: Mater. Sci. Process.* **2014**, *114*, 11−32.
(59) Purja Pun, G. P.; Mishin, Y. Development of an Interatomic Potential for the Ni-Al System. *Philos. Mag.* **2009**, *89*, 3245−3267.
(60) Becker, C. A.; Tavazza, F.; Levine, L. E. Implications of the Choice of Interatomic Potential on Calculated Planar Faults and Surface Properties in Nickel. *Philos. Mag.* **2011**, *91*, 3578−3597.
(61) Murr, L. E. *Interfacial Phenomena in Metals and Alloys*; Addison-Wesley Pub. Co., Advanced Book Program: Boston, 1975.
(62) Palik, E. D. *Handbook of Optical Constants of Solids*; Academic Press: New York, 1998.
(63) Lin, Z.; Zhigilei, L. V. Temperature Dependences of the Electron−Phonon Coupling, Electron Heat Capacity and Thermal Conductivity in Ni under Femtosecond Laser Irradiation. *Appl. Surf. Sci.* **2007**, *253*, 6295−6300.
(64) Lin, Z.; Zhigilei, L. V.; Celli, V. Electron-Phonon Coupling and Electron Heat Capacity of Metals under Conditions of Strong Electron-Phonon Nonequilibrium. *Phys. Rev. B: Condens. Matter Mater. Phys.* **2008**, *77*, 075133.
(65) Groeneveld, R. H. M.; Sprik, R.; Lagendijk, A. Femtosecond Spectroscopy of Electron-Electron and Electron-Phonon Energy Relaxation in Ag and Au. *Phys. Rev. B: Condens. Matter Mater. Phys.* **1995**, *51*, 11433−11445.
(66) Mills, K. C.; Monaghan, B. J.; Keene, B. J. Thermal Conductivities of Molten Metals: Part 1 Pure Metals. *Int. Mater. Rev.* **1996**, *41*, 209−242.
(67) Jackson, K. A. The Interface Kinetics of Crystal Growth Processes. *Interface Sci.* **2002**, *10*, 159−169.
(68) Ashkenazy, Y.; Averback, R. S. Kinetic Stages in the Crystallization of Deeply Undercooled Body-Centered-Cubic and Face-Centered-Cubic Metals. *Acta Mater.* **2010**, *58*, 524−530.
(69) Mendelev, M. I. Molecular Dynamics Simulation of Solidification and Devitrification in a One-Component System. *Modell. Simul. Mater. Sci. Eng.* **2012**, *20*, 045014.
(70) Ivanov, D. S.; Zhigilei, L. V. Effect of Pressure Relaxation on the Mechanisms of Short-Pulse Laser Melting. *Phys. Rev. Lett.* **2003**, *91*, 105701.
(71) Luo, S.-N.; Ahrens, T. J.; Çağın, T.; Strachan, A.; Goddard, W. A., III; Swift, D. C. Maximum Superheating and Undercooling: Systematics, Molecular Dynamics Simulations, and Dynamic Experiments. *Phys. Rev. B: Condens. Matter Mater. Phys.* **2003**, *68*, 134206.

DOI: 10.1021/acsnano.6b02970
ACS Nano 2016, 10, 6995−7007